Polymers & biopolymers

Destructive and non-destructive mechanical characterisation of chocolate with different levels of porosity under various modes of deformation

Dimitrios Bikos[1],* , Georgios Samaras[1], Philippa Cann[1], Marc Masen[1], Yannis Hardalupas[1], Joselio Vieira[2], Christoph Hartmann[3], Peter Huthwaite[1], Bo Lan[1], and Maria N. Charalambides[1]

[1] Department of Mechanical Engineering, Imperial College London, London, UK
[2] Nestlé Product Technology Centre, York, UK
[3] Nestlé Research Lausanne, Lausanne, Switzerland

ABSTRACT

Chocolate exhibits a complex material response under the varying mechanical loads present during oral processing. Mechanical properties such as Young's modulus and fracture stress are linked to sensorial attributes such as hardness. Apart from this link with hardness perception, these mechanical properties are important input parameters towards developing a computational model to simulate the first bite. This study aims to determine the mechanical properties of chocolate with different levels of micro-aeration, 0–15%, under varying modes of deformation. Therefore, destructive mechanical experiments under tension, compression, and flexure loading are conducted to calculate the Young's modulus, yield, and fracture stress of chocolate. The values of Young's modulus are also confirmed by independent ultrasonic mechanical experiments. The results showed that differences up to 35% were observed amongst the Young's modulus of chocolate for different mechanical experiments. This maximum difference was found to drop with increasing porosity and a negligible difference in the Young's modulus measurements amongst the different mechanical experiments is observed for the 15% micro-aerated chocolate. This phenomenon is caused by micro-pores obstructing the microscopic inelastic movement occurring from the early stages of the material's deformation. This work provides a deeper understanding of the mechanical behaviour of chocolate under different loading scenarios, which are relevant to the multiaxial loading during mastication, and the role of micro-aeration on the mechanical response of chocolate. This will further assist the food industry's understanding of the

design of chocolate products with controlled and/or improved sensory perception.

Introduction

Composites have been commonly designed and used in almost every field of engineering due to the superior material properties that they exhibit over their constituents and the relatively low specific density [1, 2]. Composites usually consist of two or more phases, at least one of each in a continuous phase. A vast literature has been devoted to study the microstructure and the interactions amongst the phases towards a reliable prediction of the effective properties [3–5] and the final performance of the composite. The geometrical parameters, such as arrangement, orientation, shape, and volume fraction of the phases, play vital role on composite's performance [4, 6, 7].

An example of composites is concrete which is widely used in variety of engineering applications due to its strength and durability [7]. The different phases and the interactions amongst the phases in concrete's microstructure are responsible for the final mechanical response under operational loads [8]. Another example of a multiphase composite is chocolate, consisting of a variety of hard particles, sugar crystals, cocoa solids, and in some cases milk powder particles, all dispersed in a continuous soft matrix of cocoa butter and in some cases milk fat [9, 10]. The weight fraction of the hard particles in chocolate typically ranges from 50 to 60 wt% [11, 12]. In micro-aerated chocolates, the micro-pores in the chocolate microstructure exist in relatively small porosity levels, i.e. up to 15%, and exhibit similar sizes to the rest of the particulates found in the chocolate [13, 14]. However, even at such low porosity levels, micro-aeration has been reported to drastically affect material and sensory properties [13, 15–18].

For chocolate at solid state, no systematic experiments have been reported to measure the mechanical properties, such as Young's modulus, yield, and fracture stresses, under different modes of deformation. In addition, no studies have been conducted to reveal the effect of micro-aeration on the chocolate's mechanical behaviour.

In foods, the computation of the mechanical properties is crucial because they drive the behaviour of the food during processes with industrial interest, such as food oral processing [19, 20] and manufacturing [21]. In oral processing, the first bite constitutes the initial stage which guides fragmentation and the release of a plethora of sensorial attributes [22]. This stage is the most crucial since it dictates the way the material will break, i.e., in a few large or multiple small fragments, coming into contact with the taste buds and mechanoreceptors in the oral cavity [23, 24]. Therefore, the fragmentation pattern influences the intensity of the sensorial attributes released during oral processing [16]. During the first bite, the food is approximately a few centimetres corresponding to a couple of grams in size [25]. At this point, bulk mechanical properties such as the Young's modulus, fracture stress and toughness determine how the material will respond under the multiaxial loading occurring by the action of the teeth [26]. These mechanical properties are reported to also influence mastication parameters such as the mastication rate and chewing forces [23].

To simulate the first bite conditions using computational models, a constitutive model is required which contains material parameters such as stress–strain data, including the Young's modulus. For an accurate representation of the material response, these material parameters should be known for different loading events such as tension and compression. More specifically, the material response under tensile conditions is often important because fracture events, in most materials, occur under tensile conditions [20]. On the other hand, the compression events are associated with the compressive action of the teeth against the food. Moreover, the significance of measuring these material properties has been highlighted not only because these properties are important input parameters to simulate various processes with industrial interest but also because they are linked to consumer perception [16, 27, 28]. More specifically, material properties such as Young's modulus and fracture stress are often linked to sensorial attributes, such as hardness [22, 23, 29, 30]. This sensory property is often reported to guide and

determine the textural profile of the material since it is perceived at the early stages of food oral processing [22, 31, 32].

Our previous work on the effect of micro-aeration on mechanical properties of chocolate gave deeper insights into the complex mechanical behaviour of the material and how micro-aeration affects the material properties, such as Young's modulus, yield and fracture stress, but only under compressive conditions [13]. Therefore, the need to establish the material properties under different modes of deformation, relevant to mastication [26], remains. It is commonly reported that the material properties of polymers, either food or otherwise, exhibit dependency on the deformation mode [33–35]. Therefore, the computation of material properties for different deformation modes and levels of porosity will be the focus of this study to fill the gap in the literature and highlight the complex material response of multiphase materials such as chocolate.

This study aims to define the mechanical properties, and specifically the yield stress, fracture stress, and Young's modulus of chocolate under varying levels of micro-aeration ranging from 0 to 15% for different modes of deformation, i.e. compression, tension, and flexure. The Young's modulus of chocolate extracted from non-destructive methods is compared against the Young's modulus computed from destructive mechanical tests under different modes of deformation. Specifically, the value of the modulus extracted by the ultrasonic methods is compared to the ones measured from the uniaxial monotonic, loading–unloading experiments in compression, tension, and three-point bending. The non-destructive method will act as an independent way to validate the value of the chocolate's modulus and potentially the assumptions proposed by Bikos et al. [13] regarding the possible microscopic plasticity that occurs from the early stages of the chocolate's deformation.

Material and methods

Materials

One non-aerated milk chocolate and two micro-aerated chocolate materials of 10% and 15% level of porosity with typical compositions were provided by Nestlé Product Technology Centre (NPTC) in York,

UK. The composition of the chocolate samples was 44%*wt* sugar crystals, 27%*wt* cocoa fats, 10%*wt* milk powders, and 6%*wt* cocoa solids. In all chocolate samples, a small percentage ($\sim$ 0.3%) of sunflower lecithin was added into the chocolate mixture. For the detailed information regarding the methodologies of the manufacturing stages and micro-aeration method of all chocolate samples, the reader is referred to Bikos et al. [13, 14].

The geometries that the chocolate samples were provided were as follows: cylindrical samples of 20 mm diameter and 20 mm height (see Fig. 1a and b) and rectangular beams of 80 mm length L, 15 mm width W and 8 mm thickness B (see Fig. 1d and f). To minimise the barrelling effect due to friction in uniaxial compression tests, the cylindrical samples were provided in a diameter to height ratio of 1:1 [36, 37]. The rectangular beam samples were used in the uniaxial tension and the three-point bending experiments.
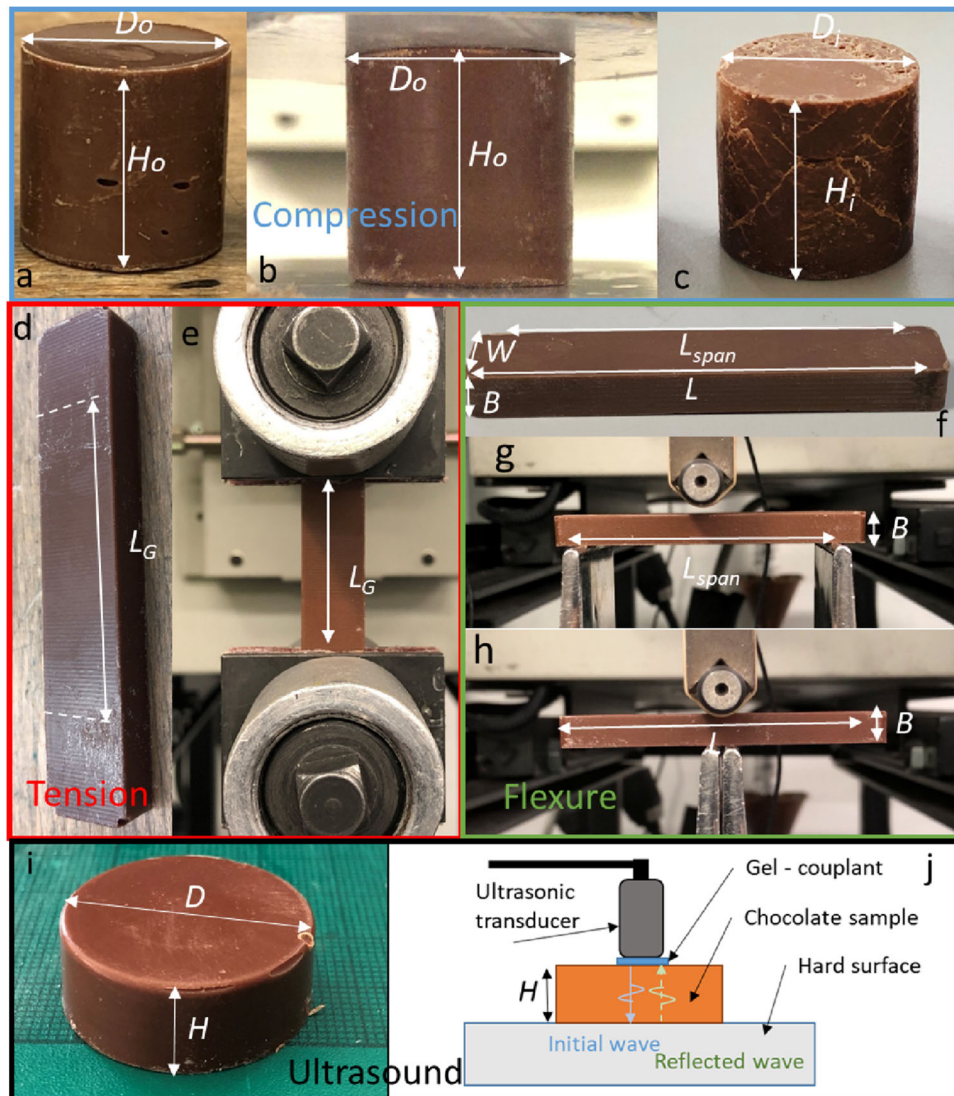
Shorter cylindrical chocolate samples with dimensions of height, H, of 10 mm and diameter, D, of 25 mm, as shown in Fig. 1i were used for the ultrasonic experiments. The shorter cylindrical samples were selected to capture a higher number of longitudinal waves.

Experimental methods

Microscopy

A Cryo-SEM stage (ALTO 2011 Gatan, UK) was connected to the Hitachi S-3400 SEM instrument to observe the microstructure of chocolate at cryogenic temperatures close to $-$190 °C. The Cryostage was placed inside the SEM chamber and the chocolate sample was inserted into the chamber through a prep chamber using a metallic rod (see Fig. 2). The chocolate sample was cooled down to $-$190 °C in the prep chamber before being placed inside the SEM chamber which was also controlled to be at the same temperature. The cooling of the chamber was achieved using liquid nitrogen.

At the prep chamber, the surface of the chocolate sample was fractured using a sharp metallic blade to remove the excessive ice formation at the surface of the sample and reveal the inner surface. To eliminate completely the ice formation, the chocolate sample was subjected to sublimation. During sublimation, the temperature of the prep chamber was raised and

Figure 1 Geometries of the chocolate samples used for the mechanical experiments together with the experimental setups. The images, which are grouped based on the type of test, show: **a** a cylindrical chocolate sample used for the compression experiments, **b** the same sample placed between the compression plates which had PTFE film attached on their surface, **c** a 15% micro-aerated chocolate sample at the end of a compression experiment with macroscopic surface cracks at 45° degrees denoting shear failure, **d** rectangular beam chocolate sample used for the tension experiments, **e**, the same sample clamped by the tensile grips **f** beam chocolate sample used for the three-point bending experiments, **g** a 10% micro-aerated chocolate sample placed on the three-point bending rig, **h** the three-point testing configuration testing the compliance of the rig and the indentation effects of the pin on the chocolate sample, **i** shorter cylindrical chocolate sample used for the ultrasonic experiments, and **j** illustration of the setup for the ultrasonic experiments.

held at -90 °C for a period of 10 min to melt the ice crystals on the sample's surface. Even though the sublimation time can have a significant impact on the final sample's structure for materials with high moisture content, this was not the case for chocolate where the water content is relatively low ($< 1\%$). The setting temperature of -90 °C together with the

holding time of 10 min was found to be typical for fat systems [38] and generally foods [39]. A gold coating was then applied by sputtering for a period of 60 s. After the completion of the sputtering, the specimen was inserted into the SEM chamber for inspection.

Figure 2 Images showing the sample preparation during the Cryo-SEM experiments. Image **a** shows the chocolate sample glued into the sample holder which in turn was connected to the metallic rod. Image **b** shows the sample connected to the rod after it was cooled to − 190 °C.
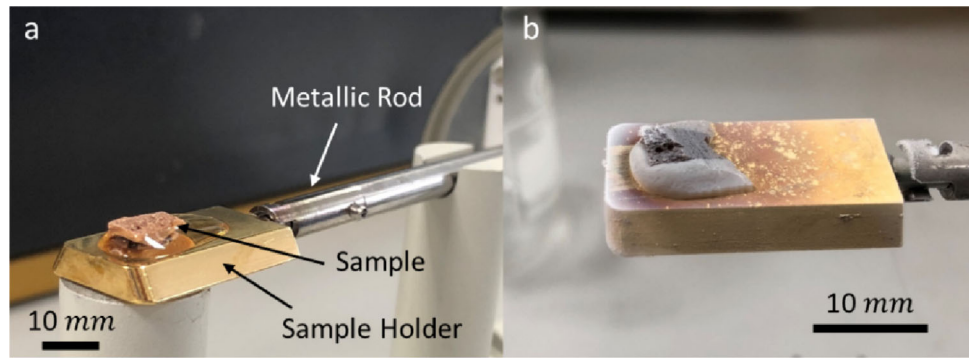
Monotonic uniaxial experiments

Monotonic uniaxial compression experiments were performed for all chocolate materials on a 5584 universal Instron testing instrument with a 2 kN load cell. The environmental testing conditions were a temperature of 20 °C and 50% humidity. These tests were performed under monotonically increasing applied strain up to fracture, i.e. up to the instant when macroscopic cracks throughout the chocolate sample were observed. Four constant true strain rates were used, i.e. $\dot{\varepsilon} = 0.001$ s^{-1}, 0.01 s^{-1}, 0.1 s^{-1} and 1 s^{-1}, which cover the mastication speed range (0.5 s^{-1}–1 s^{-1}) [40–42]. Before the compression experiments, a thin PTFE film was applied on the compression plates to minimise the friction coefficient at the chocolate-compression plate interface [36]. Compliance tests were conducted at the same strain rates by bringing the compression plates in contact with each other to measure the deflection which is not associated with the material deformation. The results showed a minor (less than 5%) effect of the machine compliance in the computed stress–strain response.

The uniaxial tensile tests were performed on the same equipment and the same environmental conditions, i.e. temperature and humidity, as the compression tests but this time a load cell of 100 N was used due to the significantly lower fracture loads experienced during these tests. The rectangular beam samples were loaded under the same four true strain rates as the compression tests until sample separation occurred. Serrated tensile grips were used to minimise any slippage effects and a gauge length of 40 mm was selected. Specimens in dumbbell shape are the recommended geometry from the ASTM standards to ensure uniform forces within the gauge region and avoid premature fracture at the grips. However, dogbone and dumbbell shapes proved

challenging to manufacture due to the chocolate's brittle nature. Therefore, the geometry shown in Fig. 1d and e was used instead.

Four repeats for each testing rate for all chocolate materials were employed for both the compression and tension experiments. Machine compliance experiments under tension were not performed since it was argued to have a similarly minor effect on the stress—strain response as in the compression experiments.

The true stress, σ, and strain, ε, for a uniaxial test (compression/tension) are calculated as follows:

$$\sigma = \frac{F}{A_i} \qquad (1)$$

$$\varepsilon = \ln \frac{H_i}{H_o} \qquad (2)$$

where F is the applied force, H_i and H_o are the current and original sample height, respectively, and A_i and A_o the current and the original cross-sectional area of the sample. The fact that chocolate indicated a Poisson's ratio close to 0.49 [13] confirms the assumption of incompressible behaviour. Based on this assumption, the current sample cross-sectional area, A_i, is calculated using Eq. 3:

$$H_i A_i = H_o A_o \qquad (3)$$

For strains lower than 3%, the definition of the true and engineering stresses and strains exhibits no difference. However, for strains higher than this threshold, the true stress–strain definition should be adopted for a representative set of the stress–strain data of chocolate. Whilst this threshold was not violated during tensile experiments, this was not true for the compression experiments (see results in Sect. "Destructive mechanical experiments").

The compressive or the tensile modulus under monotonic conditions is measured from the initial

linear part of the true $\sigma - \varepsilon$ curve adopting Eq. (4). In the case of loading–unloading conditions, the Young's modulus is obtained by the slope of the initial linear region of the unloading part of $\sigma - \varepsilon$ curve:

$$E = \frac{\sigma}{\varepsilon} \qquad (4)$$

Various definitions have been used across the literature for yield stress because often it is very difficult to identify the true yield limit. Definitions such as elastic limit, offset, and cut-off yield point ("*plastic knee*") are commonly used [43–45]. In this study, the latter definition is adopted and referred throughout the text as the macroscopic yield point (or yield stress/strain).

Three-point bending tests were conducted according to the ASTM standards [46] on the rectangular beam specimens, see Fig. 1f, to compute the flexural modulus of all types of chocolate. The chocolate was loaded in a three-point bending setup (see Fig. 1g) on a 5584 Instron with a load cell capacity of 100 N and testing conditions of 20 °C temperature and 50% humidity.

According to the ASTM standards, the suggested ratio of length span, L_{span}, to thickness, B, should be either 16:1 or 32:1. At these ratios the shear deformation, which can affect the measurements of the flexural modulus, is eliminated. However, the suggested ratios compromised the quality of the moulded chocolate samples, leading to non-flat geometries with a slight bend. Therefore, a lower ratio of 8:1 (L_{span} = 64 mm) was selected. Higher ratios of length span to thickness are usually recommended for polymers with laminar structures where the out of plane shear strength is low and the shear deformation cannot be neglected. However, using the Timoshenko beam theorem, the shear contribution to the total deflection of the beam will be measured here, as described later in this section.

For a material with a rate-dependent behaviour, the material properties extracted from a three-point bending experiment are only comparable to the compressive/tensile properties if the monotonic tests are performed under the same testing speeds and same environmental conditions. Based on the ASTM standards for synthetic polymers [46], Eq. (5) should be adopted to ensure the same strain rate is utilised for all monotonic tests.

$$\dot{\delta} = \frac{L_{\text{span}}^2}{6\text{B}} \dot{\varepsilon}_{\max} \qquad (5)$$

where $\dot{\delta}$ is the crosshead speed of the loading pin and $\dot{\varepsilon}_{\max}$ is the required maximum true strain rate at the top or bottom of the cross section of the beam. It is noted that Eq. (5) does not consider any shear contribution to the material's deformation.

Force–displacement data were recorded at three constant crosshead speeds of 0.085 mm s^{-1}, 0.85 mm s^{-1} and 8.5 mm s^{-1}. These speeds correspond to equivalent maximum strain rates of 0.001 s^{-1}, 0.01 s^{-1}, and 0.1 s^{-1} as the ones from the compression and tension tests, see Eq. (5). The speed of 85 mm s^{-1} which corresponds to the strain rate of 1 s^{-1} exceeded the maximum speed limit of the testing instrument and, therefore, was not possible. Four repeats for each testing speed for all chocolate materials were employed for these tests. In all cases, the error bars were computed to represent the entire range of the force–displacement data amongst each repeat.

In addition, a correction of the load–deflection curve was performed to consider any possible indentation of the loading pin and the supports into the chocolate as well as eliminate any machine compliance effects. To make the correction, the support pins were moved together to the mid-span below the loading pin as shown in Fig. 1h, and the chocolate was loaded up to the same force threshold as the three-point bending experiments and the same crosshead speeds. The deflection obtained by the experiment shown in Fig. 1h is subtracted by the deflection measured by the experiment of Fig. 1g, as described in detail by ASTM standards for synthetic polymers [46]. This correction requires that the deflection measurements in both experiments correspond to the same load threshold.

The flexural modulus of a material was measured using the slope $\frac{P}{\delta_b}$ in the initial linear region of the load–deflection curve:

$$E_{\text{Flexure}} = \frac{PL_{\text{span}}^3}{4\delta_b W B^3} \qquad (6)$$

where P is the mid-point load and δ_b is the mid-point displacement due to bending.

Based on the Bernoulli–Euler beam theory, the shear contribution to the material's deformation is considered negligible. To account these effects, the Timoshenko beam theory needs to be employed

where the total elastic deflection, δ_t, for a beam under bending, consists of the elastic deflection due to flexure δ_b and the elastic deflection due to shear δ_s and is described as follows:

$$\delta_t = \delta_b + \delta_s \tag{7}$$

Implementing the deflection of the beam due to shear, the elastic deflection due to flexure δ_b is given by [47]:

$$\delta_b = \delta_t - \frac{\mu_s P L_{span}}{4GA} \tag{8}$$

where G is the shear modulus, A is the cross-sectional area, and μ_s is a shape factor, which for a rectangular beam is 1.2 [47]. A value for δ_t is obtained by the three-point bending experiments. In that way, δ_b is obtained using the load–deflection data from the experiments and substituted in Eq. (6). The shear modulus is obtained from the following equation:

$$G = \frac{E}{2(1+v)} \tag{9}$$

where E is assumed to be $E_{Flexure}$ for a given testing speed and v is the Poisson's ratio which for the non-aerated and the two micro-aerated chocolates was found to be of 0.49 and 0.47, respectively [13].

In cases where $E_{compression} \neq E_{tension}$, the experienced strain rates at the surfaces of the sample are affected, as is the position of the neutral axis (Fig. 3). This results to a discrepancy in the maximum strain rates and Eq. (5) is no longer valid. The stress and strain distributions under flexure conditions are illustrated in Fig. (3). To address this, the methodology presented by Mujika et al. [48] is adopted here.

Mujika et al. [48] proposed methods to calculate $E_{compression}$ and $E_{tension}$ of unidirectional composites performing flexural experiments, either three-point or four-point bending, in cases where the two moduli are not equal. Employing a modified classical beam theory, the following relationship was formulated associating $E_{Flexure}$ and $E_{tension}$:

$$E_{Flexure} = \frac{4}{\left(1 + \sqrt{\lambda}\right)^2} E_{tension} \tag{10}$$

where λ is the ratio of $E_{tension}$ over $E_{compression}$. For the computation of the ratio λ in this study, the moduli obtained from the loading–unloading experiments described in Sect. "Loading–Unloading experiments" using the initial linear portion of the unloading part of the curve was employed. This was attributed to the fact that inelastic effects during the early stages of the material's deformation were observed [13, 14].

Since in this study the compressive and tensile moduli are already computed from uniaxial compression and tension experiments, respectively, Eq. (10) was used to assess the agreement to the flexural modulus obtained from the destructive three-point bending experiments, see Eq. (6).

Based on Mujika et al. [48], the material thickness under compression, $B_{compression}$, and tension, $B_{tension}$, during three-point bending conditions can be computed using:

$$B_{tension} = \frac{B}{1 + \sqrt{\lambda}} \tag{11}$$

$$B_{compression} = \frac{B\sqrt{\lambda}}{1 + \sqrt{\lambda}} \tag{12}$$
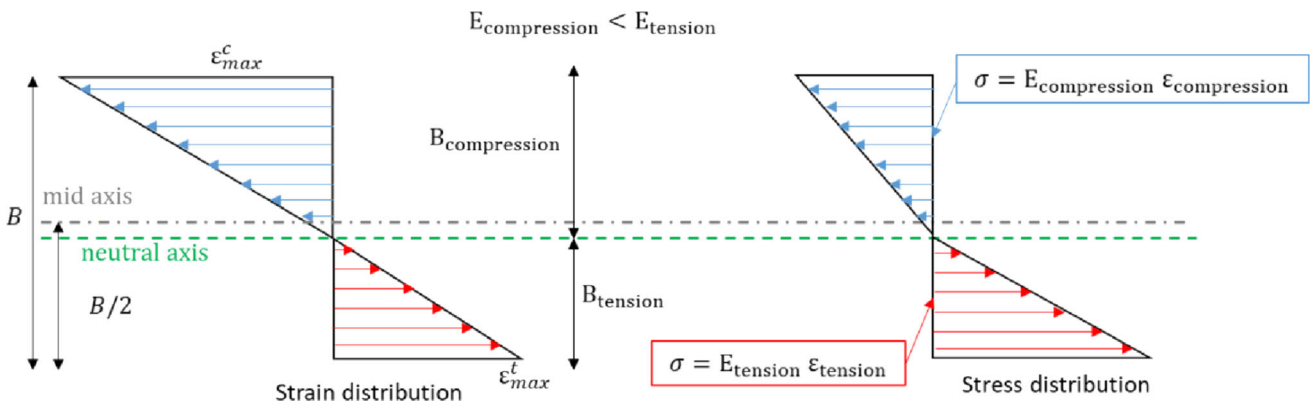
Figure 3 Schematic showing the distribution of the compressive, in blue colour, and tensile distributions, in red colour, in terms of strains and stresses across the thickness, B, of the chocolate sample.

where B is the total thickness of the beam specimen, see Fig. 1f.

The maximum tensile strain, ε_{max}^t, and stress, σ_{max}^t, are given by:

$$\varepsilon_{max}^t = \frac{\sigma_{max}^t}{E_{tension}} \tag{13}$$

$$\sigma_{max}^t = \frac{M}{\beta I}B_{tension} = \frac{PL_{span}}{\beta 4I}B_{tension} \tag{14}$$

where I is the second moment of area, and β is the ratio equal to $4/\left(1+\sqrt{\lambda}\right)^2$.

Similarly, the compressive maximum stress, σ_{max}^c is given by:

$$\sigma_{max}^c = \frac{M}{\lambda\beta I}B_{compression} = \frac{PL_{span}}{\lambda\beta 4I}B_{compression} \tag{15}$$

Combining Eqs. (6), (10), (13), and (14), the following equation is derived for the maximum strain at the bottom surface of the beam:

$$\varepsilon_{max}^t = \frac{12B_{tension}}{L_{span}^2}\delta_b \tag{16}$$

Equation (16) can be used to calculate the maximum compressive strain at the top surface, ε_{max}^c, of the beam if $B_{tension}$ is substituted by $B_{compression}$. Equation (16) reduces to Eq. (5) when it is differentiated with respect to time and assuming that the neutral axis is at the centre of the beam, and hence, $B_{tension} = B/2$.

Once the location of the neutral axis is defined using Eqs. (11) and (12), the maximum tensile strain rate at the bottom of the chocolate beam during three-point bending conditions can be calculated by differentiating Eq. (16) (and similarly for the maximum compressive strain rate at the top of the chocolate beam). This methodology was performed for all chocolate porosities, i.e. 0%, 10%, and 15%.

It should be noted that Eqs. (13)–(15) correspond to the engineering stresses and strains (as opposed to true stresses and strains) under flexure. However, this is argued not to be an issue since the maximum applied strains calculated by Eq. (16) led to strains well below the 3% limit. Therefore, the stress–strain data obtained using this methodology are comparable to the data obtained from the compression and tension experiments.

Finally, the Hashin–Shtrikman upper bound was employed to provide a comparison between the analytical and experimental values of the Young's modulus of chocolate as a function of porosity. Based on the Hashin–Shtrikman analytical model, the bulk modulus k and shear modulus G of the porous chocolate are calculated as:

$$k = \frac{4(1-f)k_mG_m}{4G_m + 3fk_m} \tag{17}$$

$$G = \frac{(1-f)(9k_m + 8G_m)G_m}{4G_m(2+3f) + 3k_m(3+2f)} \tag{18}$$

where f, k_m, and G_m are the porosity, bulk and shear modulus of the chocolate. The Young's modulus, E, is then calculated by:

$$E = \frac{9kG}{3k + G} \tag{19}$$

In this study, the Young's modulus calculated from Eq. (19) for different values of porosity is compared against an average value of Young's modulus measured from the different types of mechanical experiments for each type of chocolate.

Loading–unloading experiments

For various soft foods, such as cheese and dough, no clear initial linear region is observed in the $\sigma - \varepsilon$ curve [36, 49], and therefore, the calculation of the Young's modulus is assumed to be subjective. In biomaterials, such as bones, even though they exhibit a clear linear initial region, the Young's modulus is suggested to be quoted from loading–unloading curves and specifically from the initial linear part during unloading [50, 51]. For this reason, loading–unloading tests in compression mode at a constant true strain rate of 0.01 s^{-1} were performed for different maximum applied strain values.

In the case of the non-aerated chocolate, three maximum applied strains were arbitrary selected as 0.015, 0.025, 0.045 followed by a strain removal until the zero-force position. On the other hand, the two micro-aerated chocolate samples were subjected to two maximum strains of 0.01, 0.025 for 10% and 0.04, 0.025 for 15% porosities. All selected strain thresholds were arbitrary selected, except for one strain threshold for each chocolate variety which was selected to within the initial linear region based on preliminary loading–unloading experiments. Strain rates higher than 0.01 s^{-1} were not employed due to limitations observed from the instrument in effectively

controlling the motor to reach the target strain. Loading–unloading tests were repeated at a slower strain rate of 0.001 s^{-1} and the same strain levels as the tests at 0.01 s^{-1} to investigate any rate dependence of the Young's modulus evaluated from the unloading slopes.

Similarly, loading–unloading tests in tension mode were conducted on the same types of chocolate under smaller maximum applied strains than in the compression tests due to the smaller fracture strains experienced under tensile load. Based on preliminary experiments, there was no permanent deformation prior to failure in tension, and therefore, the strains were limited to within the initial linear region of the stress–strain curve. The 0% and 15% micro-aerated chocolate samples were loaded up to a maximum strain of 0.0007 at a constant strain rate of 0.01 s^{-1}, followed by a removal of the applied strain to the zero-force position. The 15% micro-aerated chocolate was loaded up to a strain of 0.0005. Four repeats were used for each chocolate sample for each type of experiment.

In the case of the non-aerated chocolate, the loading–unloading experiments in flexure were performed using two maximum deflections of 0.2 mm and 0.3 mm at a constant speed of 0.85 mm s^{-1}, which is equivalent to the strain rate of 0.01 s^{-1} in compression and tension, followed by a load reversal to the zero-force position. On the other hand, the 10% and 15% chocolate were deformed to maximum deflection levels of 0.15 mm and 0.2 mm under 0.85 mm s^{-1}. All experiments were repeated three times for each porosity and each testing condition. Compliance tests were also employed to estimate the true load–deflection curve in all cases.

*Non-destructive ultrasonic tests (NDT)*

Ultrasonic experiments were employed on the 0%, 10%, and 15% porosity chocolate, to calculate the Young's modulus and compare it against the one calculated from the various destructive mechanical experiments described in Sect. "Monotonic uniaxial experiments" and "Loading–Unloading experiments".

A typical setup for ultrasonic experiments consists of an ultrasonic wave transducer, see Fig. 1j, which is connected in an ultrasonic pulse-receiver connected in turn to a digital oscilloscope. To enhance the quality of the experimental measurements, ultrasound transmission gel was applied between the chocolate sample and the transducer, see Fig. 1j. The gel was used to enhance coupling between the transducer and the chocolate; its acoustic impedance is more closely matched to both the chocolate and the transducer than any trapped air which could otherwise exist at the interface. A frequency of 1 *MHz* was used for these experiments. This selected frequency was found to create the clearest wave signal based on preliminary experiments (results not shown). The environmental conditions were selected to be the same as the destructive mechanical tests, i.e. temperature of 20 °C and relative humidity of 50%. All experiments were repeated twice.

A typical amplitude–time graph in the case of non-aerated chocolate is shown in Fig. 4. The graph consists of three main pulses, the excitation pulse passing through the transducer, the first and the second ultrasound waves passing through the chocolate sample. The time between two maximum peaks between two consecutive waves constitutes the Time of Flight (ToF) which depends on the material's elastic properties and is used to calculate the ultrasound velocity, c. The ratio between the maximum amplitudes, e.g. A_0 and A_1 see Fig. 4, between consecutive ultrasound waves is the attenuation, which is another characteristic of the ultrasound wave, but not within the scope of the present study.

The ultrasound velocity, c, is calculated from:
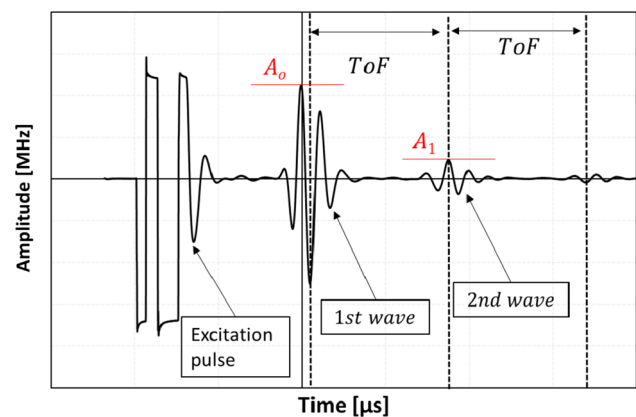
Figure 4 Typical amplitude-time plots for the non-aerated chocolate showing the excitation pulse, the first and the second ultrasonic pulse, and the definition of the time of flight (ToF) when passing through the sample. A_0 and A_1 are the maximum amplitudes of the first and second ultrasound waves, respectively.

$$c = \frac{2H}{\text{ToF}} \qquad (20)$$

where H is the height of the material.

The wavelength of sound, λ_u, is associated with the ultrasound velocity, c, and the applied frequency from the transducer, f_t, as follows:

$$\lambda_u = \frac{c}{f_t} \qquad (21)$$

The adiabatic bulk modulus or the primary wave (p-wave) modulus, B_p, for a three-dimensional solid can be calculated from the ultrasonic experiments and is related to c and the material's density, ρ, as follows [52, 53]:

$$B_p = c^2 \rho \qquad (22)$$

The Young's modulus, E, is linked to B_p, through the Poisson's ratio, v, as follows:

$$E = \frac{B_p(1 - 2v)(1 + v)}{(1 - v)} \qquad (23)$$

Equation (23) is used to convert the adiabatic bulk modulus measurements to Young's modulus. The resulting data are compared against the Young's modulus values obtained from the destructive mechanical tests.

Experimental results

Scanning Electron Microscopy experiments

Figure 5 shows the microstructure of the non-aerated (Fig. 5a and c) and the 10% micro-aerated chocolate (Fig. 5b and d) samples through the cryostage scanning electron microscope (cryo-SEM) under different magnifications. At both magnifications, a large number of irregular shaped particles, depicted in red arrows in the figure, are dispersed in the chocolate matrix, i.e. the cocoa butter. Based on the relatively high volume fraction of sugar particles ($\sim$ 50%), it is assumed that these are predominantly sugar particles.

From Fig. 5c and d, the micro-pores, which exhibit an average size of 40 μm [13, 14] and thus similar in size to the rest of the constituents in chocolate [9, 54], are randomly dispersed in the chocolate matrix. No pore agglomeration was observed from the microscopy images. For all porosities, a few random cracks were observed at the interface of the constituents, e.g. at the hard particles or at the pores' interfaces. However, these cracks are consistent with reports from the literature [21] and are not responsible for any potential difference in material properties amongst the different types of chocolate.

Figure 5 Microscopy images through the Cryostage SEM for the non-aerated (0%) and the 10% micro-aerated (10%) chocolate under different magnifications. Images show the microstructure of **a** the 0% chocolate at 500 × magnification, **b** 10% chocolate at 500 × magnification, **c** 0% at 1000 × magnification, and **d** 10% at 600 × magnification. The red arrows in all images depict the hard particles, possibly sugars, cocoa and milk solids dispersed in cocoa butter.
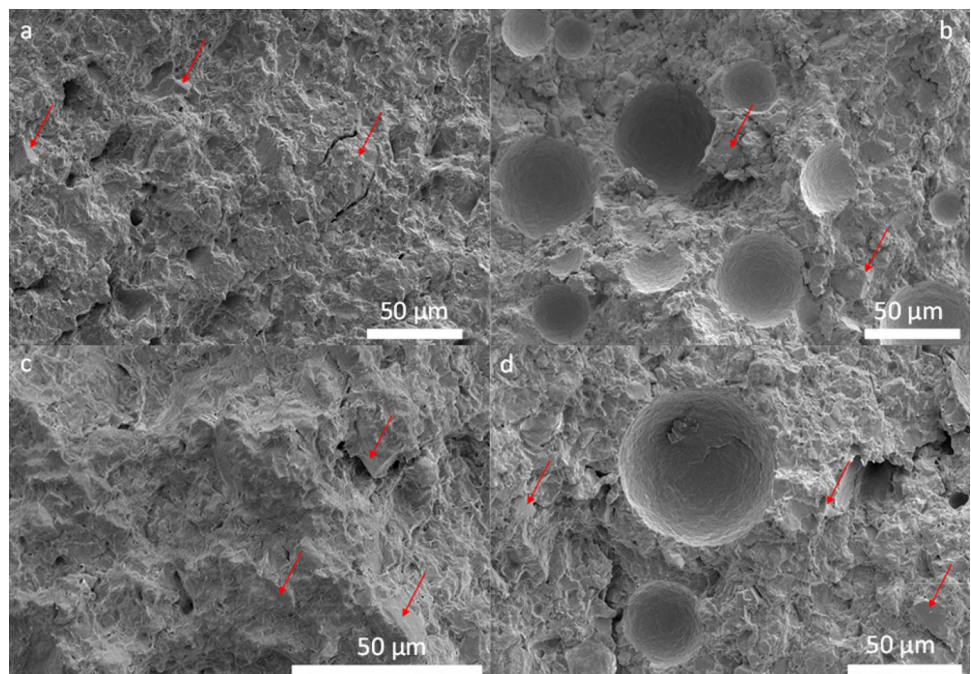
Destructive mechanical experiments

Figure 6a–c shows the combined stress–strain plots extracted from the monotonic uniaxial compression and tension experiments. Based on these plots, chocolate cannot withstand high tensile stresses and fractures at significantly lower strains compared to the fracture strains in compression. Therefore, a brittle fracture with no significant plasticity under tensile loads can be assumed for all chocolate

materials, a behaviour which is reported for other brittle materials such as concrete and cast iron [55]. On the other hand, a clear shear failure model was observed for all chocolate varieties during compression, as denoted by the shear bands at 45° degrees.

Comparing the stress–strain response between compression and tension, the difference in the maximum stress point at the highest $\dot{\varepsilon}$ (1 s^{-1}) is approximately 340%, 410%, and 480% for the 0%, 10%, and 15% micro-aerated chocolate, respectively. Therefore,
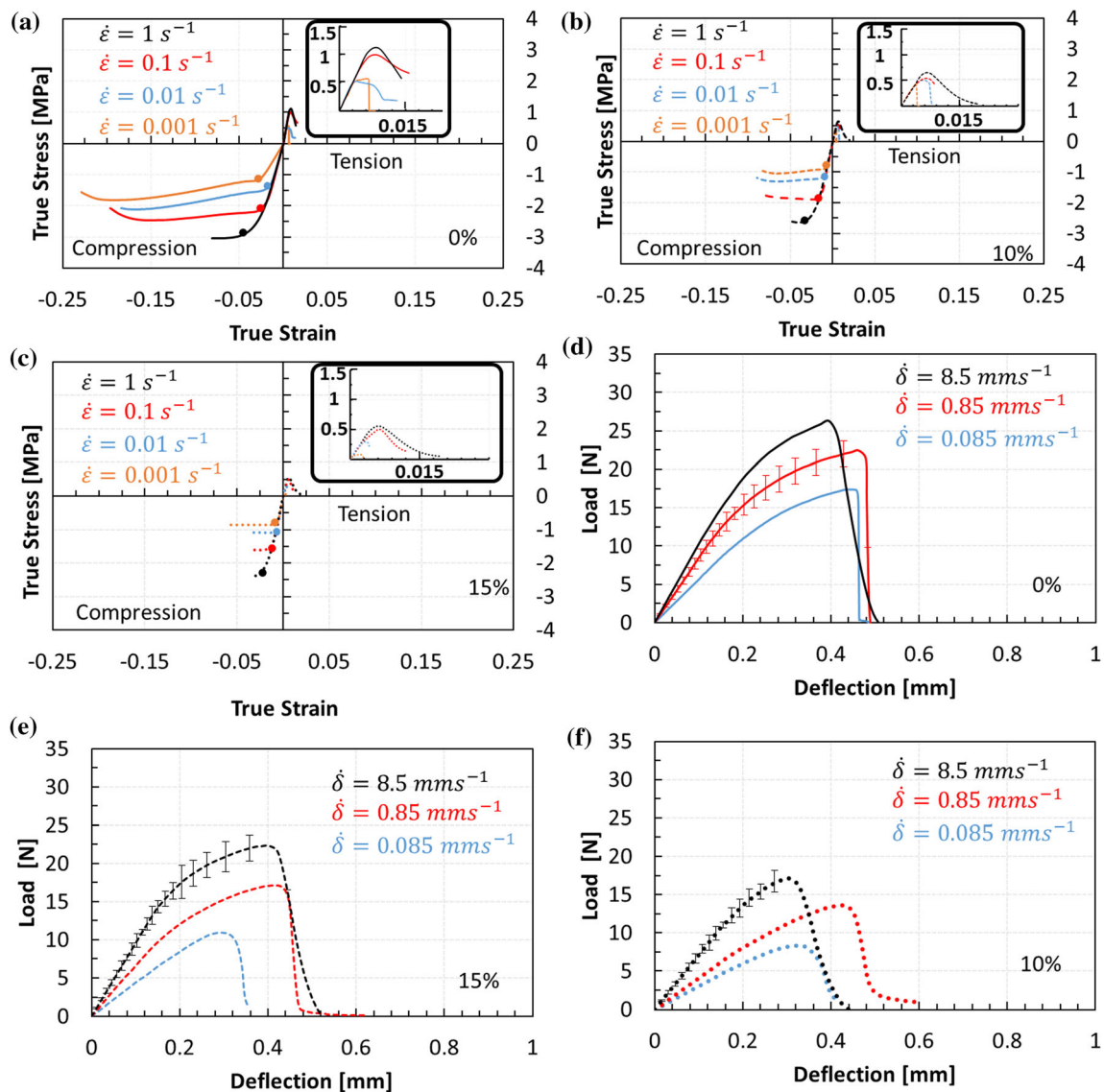
Figure 6 Monotonic uniaxial mechanical tests for all chocolate materials under different modes of deformation, i.e. compression, tension, and flexure. The graphs show: the combined stress–strain data from compression and tension in the case of the **a** non-aerated (0%), **b** 10% micro-aerated, **c** 15% micro-aerated chocolate. The load–deflection data obtained from the three-point bending experiments in the case of the **d** non-aerated (0%), **e** 10% micro-aerated, and **f** 15% micro-aerated chocolate. The micrographs in plots (**a**), (**b**), and (**c**) are magnified images of the tensile σ–ε curves and the circles indicate the macroscopic compressive yield point.

this difference between the two modes of deformation rises with increasing porosity. This is caused by the presence of the pores in the two micro-aerated chocolates which enhance the brittle nature of the material. Such differences have been reported for other materials such as concrete where differences up to an order of magnitude were reported [8, 56]. Differences of similar magnitude have been observed for other particulate composites, metallic and non-metallic, where the tensile strength was found to be 100% lower than the compressive strength [57] and even a magnitude higher for certain polymeric composites [58]. In addition, no severe discontinuity is observed in the origin of all graphs presented in Fig. 6a–c, with the tensile modulus being higher than the compressive modulus by 35% for the 0% chocolate. This difference decreases with increasing micro-aeration.

Figure 6d–f shows the average load–deflection response for all three chocolate materials under three different testing speeds of 0.085 mm s^{-1}, 0.85 mm s^{-1}, and 8.5 mm s^{-1}. A nonlinear load–deflection response was observed in all cases. It was unclear from the macroscopic observation of the fractured surfaces whether this nonlinearity is caused by plastic deformation. This is because the two fractured sample pieces perfectly matched when they were placed together after the bending experiment. However, computations of the critical bending load where material will start yielding either in tension (see Eq. 14) or compression (see Eq. 15) showed permanent plastic deformations prior to fracture in the tensile part of the cross section. More specifically, the values of the tensile fracture stress (see Fig. 7b) and compressive yield stress (see Fig. 7a) at maximum strain rates of 0.001 s^{-1}, 0.01 s^{-1}, and 0.1 s^{-1} were employed in Eqs. 14 and 15 to find the critical loads where material is expected to yield at corresponding testing speeds of 0.085 mm s^{-1}, 0.85 mm s^{-1}, and 8.5 mm s^{-1}, respectively. Regardless of the testing speed and the type of chocolate, plastic deformations are expected at the bottom part of the chocolate beam where tensile loadings occur. Therefore, the computation of the flexural stress–strain curves was not straightforward and hence, not included in this work. Since the bending events are believed to be insignificant during the first bite conditions, the computation of the flexural stress–strain data was found to exceed the scope of the current study.

In the case of the three-point bending, the scatter amongst the replicate tests is shown because a higher variability ($< 10\%$) amongst the samples was observed as opposed to the compression and the tensile experiments, which showed little scatter, and hence, no error bars are displayed. Specifically, a maximum difference of 9% is observed amongst the replicates in the case of the non-aerated chocolate, whilst the repeats for the 10% and 15% micro-aerated samples showed a variation of 7% and 9%, respectively. The error bars with the highest magnitude are shown in Fig. 6d–f for each chocolate. These differences refer to the corrected load–deflection curves after considering potential indentation or/and machine compliance effects. The corrected deflection measurement (see Fig. 1h) was found to be around 25% lower than the ones measured by the instrument (see Fig. 1g). The machine compliance and indentation, hence, were found to have a higher impact on three-point bending experiments than the compression experiments. The higher correction observed in the flexure experiments was attributed to the indentation effect of the loading pins onto the surface of the chocolate samples. The shear effect (see Eq. 8), on the other hand, was found to correspond to a correction of 5% in stiffness (0% chocolate, 8.5 mm s^{-1}) which is lower than the experimental error bars, and therefore, the shear contribution to the bending behaviour of chocolate is negligible.

The flexure load increases nonlinearly, up to a maximum load followed by a drop to zero load, implying complete fracture of the surfaces. At the lowest testing speeds, the cracked surfaces remained in contact, implying the presence of an adhesion force that holds the two cracked surfaces together, even when the samples reached the zero-force position. No clear dependence of the deflection on fracture and testing speed was reported. On the other hand, a clear decrease in the maximum force with decreasing testing speed was depicted for all types of chocolate.

Figure 7a and b shows the compressive macroscopic yield stress plotted as a function of $\dot{\varepsilon}$ (see circles in Fig. 6a–c), along with the fracture stresses (maximum stress points in Fig. 6a–) in compression and tension for all types of chocolate. No significant rate-dependent behaviour can be assumed for fracture stress under tensile conditions for all porosities. On the contrary, the compressive macroscopic yield stress and compressive fracture stress data exhibit rate-dependent behaviour. Moreover, a decrease in
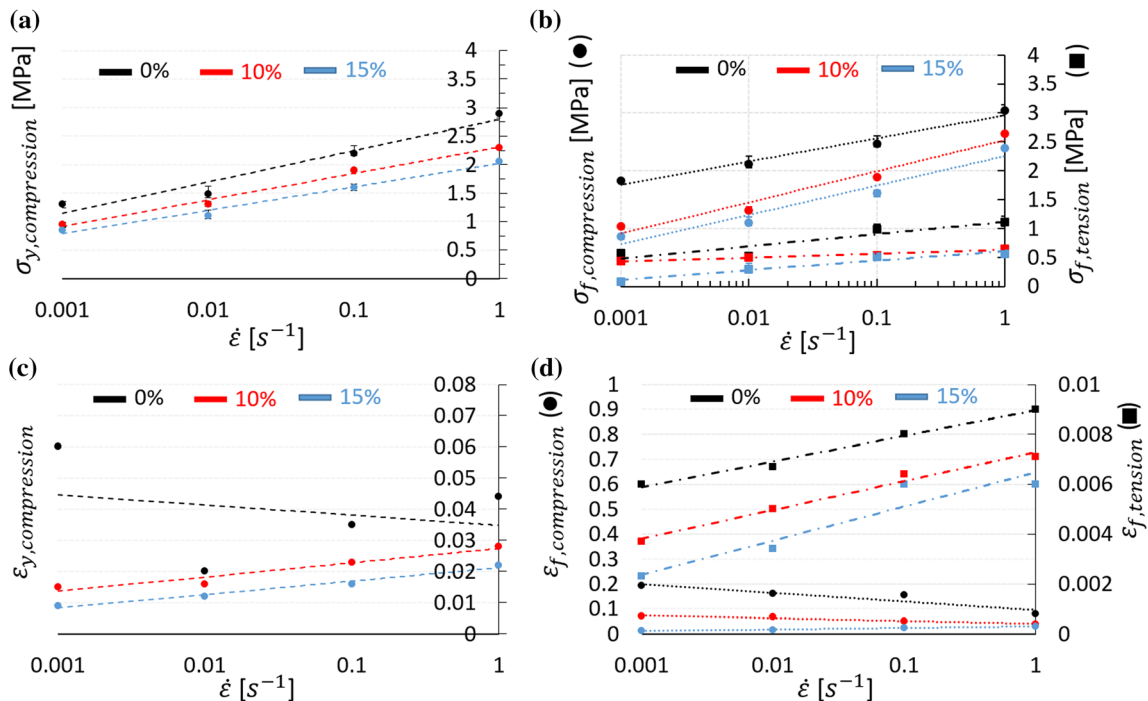
Figure 7 Graphs summarising the yield and fracture data from compression and tension experiments for all types of chocolate. Image **a** shows the macroscopic compressive yield stress as a function of rate for the 0%, 10% and 15% micro-aerated chocolate, **b** shows the fracture stress data in compression and tension (double vertical axis) for different types of chocolate, **c** the macroscopic yield strain–strain rate plot for all types of chocolate, and **d** the strains at fracture, both in compression and tension (double vertical axis), in relation to the strain rate.

the stress data, either yield or fracture, with increasing porosity is depicted for all testing rates. The latter is aligned with reports on other porous materials [59–62]. On the other hand, Fig. 7c and d presents the compressive macroscopic yield strain data as a function of strain rate (Fig. 7c), together with the fracture strains (Fig. 7d) under compressive and tensile conditions. No clear rate-dependency can be assumed for yield strain (see Fig. 7c) for the non-aerated chocolate, as opposed to fracture strains in compression for the same material (see Fig. 7d), which exhibit decreasing trends with strain rate as expected. On the other hand, a clear increasing and decreasing trend of yield (see Fig. 7c) and fracture strains (see Fig. 7d) in compression with rate, respectively, are observed for both micro-aerated materials. Interestingly, fracture strains in compression and tension exhibit opposite trends, i.e., decreasing vs increasing trends, with strain rate. This is true for all types of chocolate. The drastic difference between tensile and compressive fracture strains, shown in Fig. 7d, agrees with the literature

stating that materials fracture due to tension under multiaxial loadings [20].

In polymers, yielding occurs due to the sliding of the molecules in the polymeric chain whilst metals or other engineering materials this phenomenon is caused by the dislocations of grains causing inelastic deformations. It is argued here that chocolate could show a combination of both of these deformation mechanisms. Cocoa butter inside the chocolate consists of large chains of triacylglycerols but also exhibits hard particles such as cocoa solids and sugar crystals. The microscopic movement of these hard particulates could also cause inelastic phenomena, i.e., yielding.

Figure 8a–c summarises the stress–strain plots extracted from the loading–unloading tests in compression. Overall steeper slopes in the linear part of the unloading path compared to the ones obtained from the initial linear part of the curve corresponding to the loading stage. This is an indication of viscoelastic effects or other energy dissipation mechanisms, or potentially a microstructural movement. This effect will be further discussed shortly when the

Figure 8 Loading–unloading uniaxial mechanical tests for different chocolate varieties under compression and tensile conditions. The graphs show: the stress–strain data from the loading–unloading experiments in compression for the **a** non-aerated (0%), **b** 10% micro-aerated, and **c** 15% micro-aerated chocolate, and in tension for the **d** non-aerated (0%), **e** 10% micro-aerated, and **f** 15% micro-aerated chocolate.
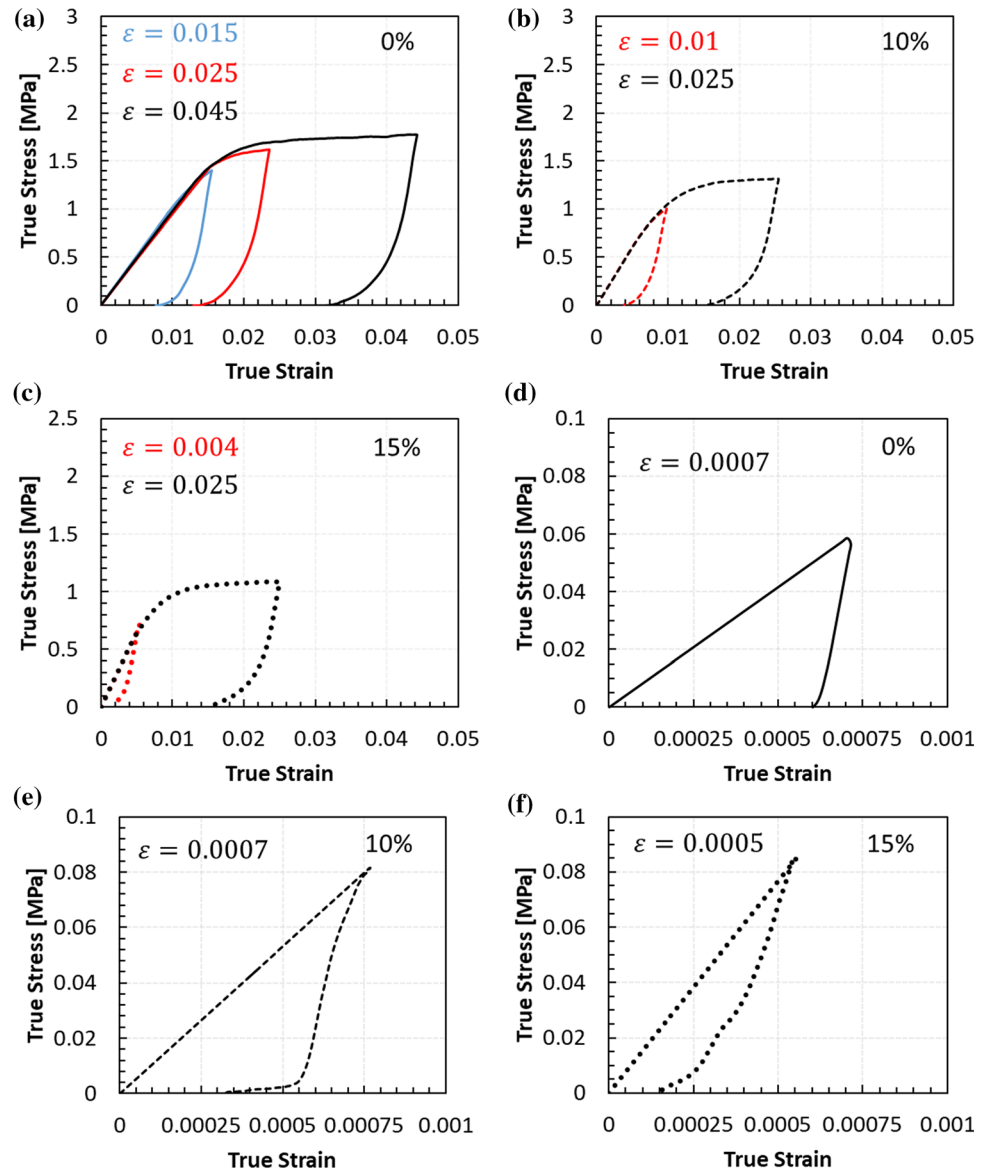
Young's modulus obtained from the different mechanical experiments is presented.

The stress–strain plots obtained from the cyclic tests in tension are summarised in Fig. 8d–f. For all tested materials, when small elastic strains of 0.0007, 0.0007 and 0.0005 were applied to the 0%, 10% and 15% porosity chocolate, respectively, and then removed, the loading and unloading paths did not coincide as would be expected for linear elastic materials. Even when time was allowed after completion of the compression tests, the tested samples did not return to their original height implying significant permanent deformations. This implies that significant inelastic permanent strains are experienced in these materials, even though the samples

were loaded to well within the initial linear region of the stress–strain curve.

Such inelastic phenomena from the early stages of mechanical deformation have been reported in the past for other materials, such as fats, bones, and other biopolymers [50, 51, 63, 64]. Based on such indications, the elastic modulus should be quoted from the linear region of the unloading part of the curve. The reason is that in highly dissipative materials, it is not always clear which portion of the curve is recoverable and directly linked to the material's elasticity. More specifically in fats, plastic structural movements of the microstructural features occur which leads to inelastic effects from the beginning of the material's

deformation. Therefore, similar arguments are posed here for chocolate.

The load–deflection graphs from the loading–unloading experiments in the three-point bending for all types of chocolate are presented in Fig. 9. In contrast to the loading–unloading tests in compression and tension, the slope at the two parts of the curves, which is the initial linear region during loading and unloading, seems to be very similar in most cases, especially for the 0% and 10% porosities. A clear difference was observed in the two slopes for the 15% micro-aerated chocolate, see Fig. 9. This effect implies smaller permanent deformations during flexure as opposed to the tensile and compression data shown in Fig. 8.

## Comparison of Young's modulus amongst different deformation modes

For a quantitative comparison, the Young's modulus measured from the various destructive mechanical tests together with the modulus measured from ultrasound experiments is summarised in Figs. 10, 11, and 12, for the non-aerated, the 10% micro-aerated, and 15% micro-aerated chocolate, respectively. For a valid comparison, the results from all materials are compared at a strain rate of 0.01 s^{-1}, where there are available data for all types of tests, monotonic and

cyclic and for every mode of deformation, tension, compression, and flexure, as well from ultrasound testing (NDT). The Young's modulus during loading–unloading in compression and tension is also presented at a constant strain rate of 0.001 s^{-1} to highlight any potential rate-dependent effects of the elastic modulus.

It is important to highlight that the Young's modulus obtained from ultrasonic experiments is not directly equivalent to the testing strain rates from the destructive mechanical experiments. For the sake of comparison between the modulus values from the two types of experiments, destructive and non-destructive, the Young's modulus from the ultrasonic experiments was assumed to be independent of frequency for all chocolates. This argument was found to have merits based on preliminary results on the tested materials with varying applied frequency from 1 to 5 MHz (results are not shown).

Figure 10 summarises the Young's modulus values for the non-aerated chocolate which are obtained from mechanical tests, destructive and non-destructive for various deformation modes and loading histories. Based on the same figure, the modulus data obtained from monotonic experiments such as tension and compression are significantly lower than the rest of the data due to early inelastic effects during the first loading cycle. Interestingly, the flexural


Figure 9 Typical load–deflection plots from loading–unloading three-point bending test for all chocolate materials at a constant speed of $\dot{\delta} = 0.85$ mm s^{-1}. Plots show load deflection data of the: **a** non-aerated chocolate ($\delta_{max} = 0.25$ mm), **b** the 10% micro-aerated chocolate ($\delta_{max} = 0.25$ mm), **c** 15% micro-aerated chocolate ($\delta_{max} = 0.15$ mm).
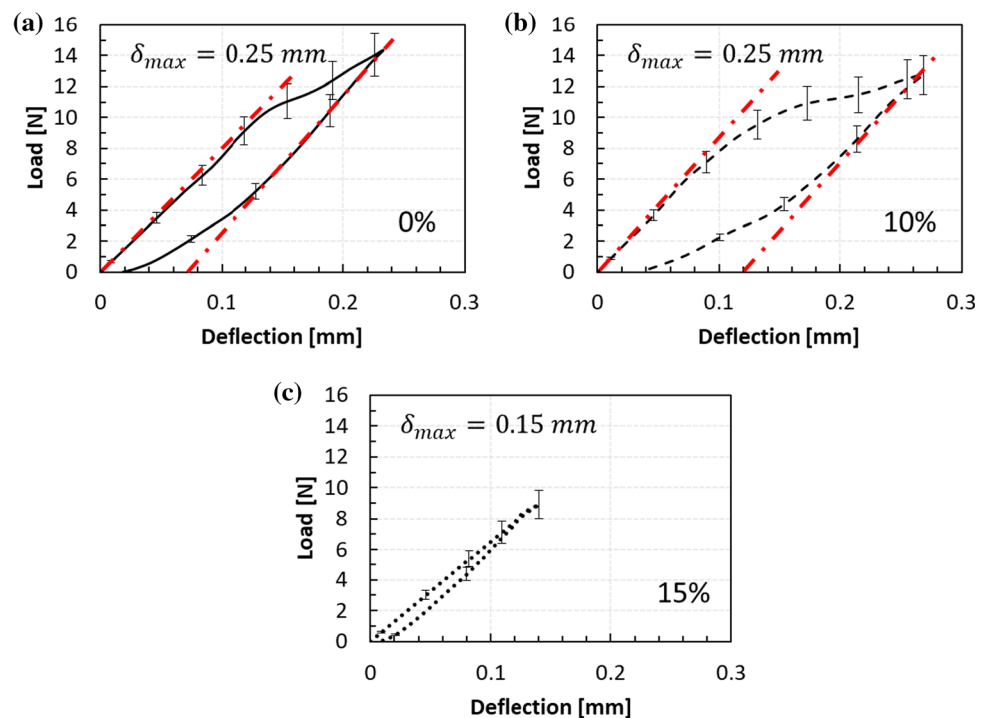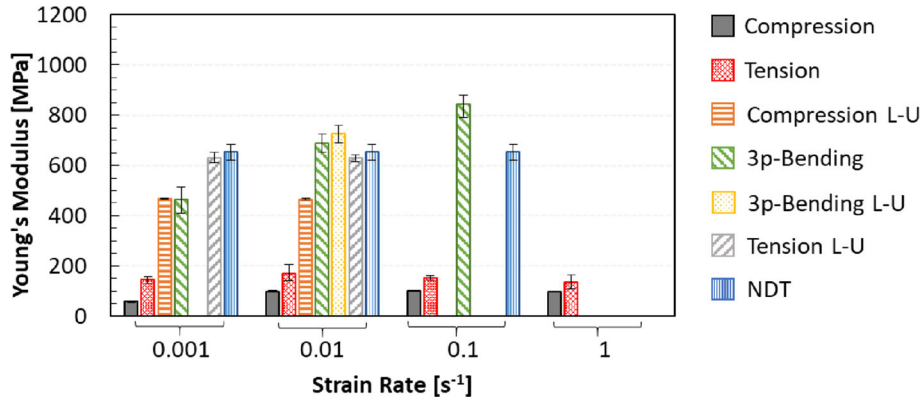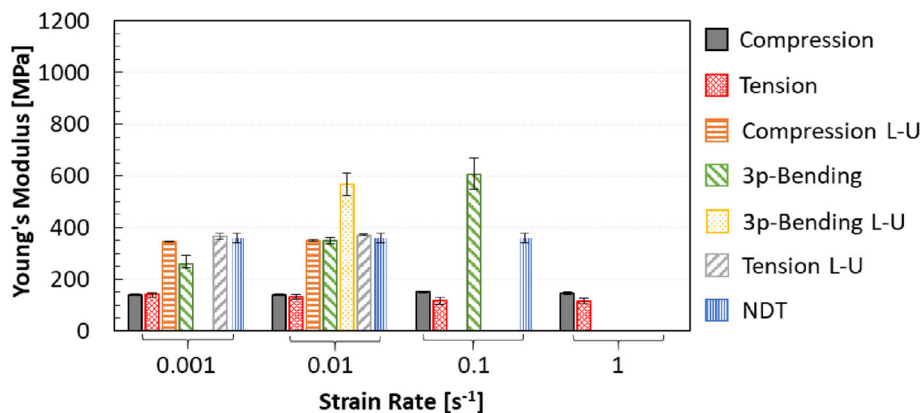
Figure 10 Average values of Young's modulus for the non-aerated chocolate obtained from different mechanical experiments; tension, compression, loading–unloading (L–U) in compression, tension and flexure, three-point bending and ultrasound (NDT). Flexural modulus is calculated using Eq. (6) for both the monotonic and L-U tests. The labels depict the average values.
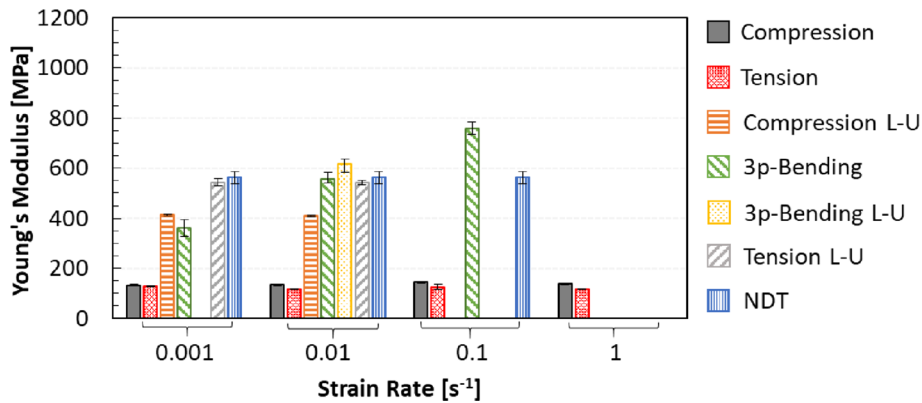
Figure 11 Average values of Young's modulus for the 10% micro-aerated chocolate obtained from different mechanical experiments; tension, compression, loading–unloading (L–U) in compression, tension, and flexure, three-point bending, and ultrasound (NDT). Flexural modulus is calculated using Eq. (6) for both the monotonic and L–U tests. The labels depict the average values.

Figure 12 Average values of Young's modulus for the 15% micro-aerated chocolate obtained from different mechanical experiments; tension, compression, loading–unloading (L–U) in compression, tension and flexure, three-point bending, and ultrasound (NDT). Flexural modulus is calculated using Eq. (6) for both the monotonic and L–U tests. The labels depict the average values.

modulus from the monotonic three-point bending tests is relatively close to the modulus values obtained from the loading–unloading tests in compression and tension but also the ultrasound experiments.

The compressive modulus at $\dot{\varepsilon}$=0.01 s^{-1} from the loading–unloading experiments (465 MPa) is smaller than the one predicted from tensile loading–unloading tests (628 MPa) and smaller than the flexural modulus (688 MPa), which in turn is of similar value to the modulus from the NDT tests (653 MPa). Adopting this order in the modulus values from the various mechanical tests, the differences in the Young's modulus between each type of test are approximately 35%, 10%, and 5%, respectively. This difference in moduli amongst the different mechanical tests decreases at the slowest strain rate of 0.001 s^{-1}, i.e. 0.6%, 36%, and 3.5%, see Fig. 10. In addition, the values of Young's modulus between three-point bending tests under monotonic and loading–unloading deformation are in good agreement.

The fact that the Young's modulus of the non-aerated chocolate between compression and tension differs creates an asymmetric effect in the maximum strains under three-point bending conditions. This asymmetric effect leads to strain rates which might be different than the one applied, i.e., 0.01 s^{-1}. Adopting the methodology presented in Sect. "Microscopy", the strain rates due to this asymmetric effect can be computed. For the non-aerated chocolate, the maximum strain rates deviated from the applied strain rate of 0.01 s^{-1} only by 10%, which led to the conclusion that the comparison amongst the modulus values from the mechanical tests, i.e., compression, tension, and flexure, at a strain rate of 0.01 s^{-1} was valid. This was found to be true also for the two micro-aerated materials. Based on Fig. 10, a clear rate-dependency in the Young's modulus is only observed by the three-point bending tests whilst the monotonic tests for all testing rates and the loading–unloading tests in compression and tension, at least at the two slowest rates, do not depict such a time-dependency.

Figure 11 summarises the Young's modulus for the 10% micro-aerated chocolate. A similar trend to the one shown in the non-aerated chocolate is also indicated. The Young's modulus at 0.01 s^{-1} is almost the same obtained by the three-point bending, loading–unloading in tension, and the NDT experiments. The

differences for this porosity amongst loading–unloading in compression vs three-point bending vs loading–unloading in tension vs NDT experiments, is 33%, 3%, and 1%, respectively. The moduli obtained from the monotonic and loading–unloading tests in flexure are in agreement, as shown in the same figure at 0.01 s^{-1}.

The Young's modulus for the 15% micro-aerated chocolate obtained from the various mechanical tests is shown in Fig. 12. Examining the data at a strain rate of 0.01 s^{-1}, a smaller discrepancy in the moduli from all types of experiments is shown compared to the other two chocolate materials. Specifically, a Young's modulus of 350 MPa, 350 MPa, 371 MPa, and 360 MPa was computed from loading–unloading experiments in compression, three-point bending, loading–unloading in tension, and NDT experiments, respectively. The maximum differences in the modulus values from these tests is 6% and the compressive (L-U) and flexural modulus match perfectly. However, a significant difference ($\sim$ 35%) in the modulus data as obtained from monotonic and loading–unloading flexure experiments is depicted, see Figs. 9c and 12.

Comparing the results of Figs. 10, 11, and 12, micro-pores are believed to eliminate any differences observed amongst the Young's modulus values from the different modes of deformation, i.e. tension (L-U), compression (L-U), and flexure, creating a material with a single stiffness value under any loading condition. More specifically, the micro-pores, when they are high enough by volume fraction, might be able to disrupt the microstructural movement of the various components found in the chocolate, which is argued earlier in this section to be dependent on the mode of deformation. However, the mechanism which creates the non-aerated chocolate's stiffness to change under different loading conditions remains unknown. In-situ mechanical tests in a scanning electron microscope (SEM) might shed further insight into the microstructural differences under varying loading conditions.

The difference in the elastic modulus from different modes of deformation has been widely reported in the literature for other materials such as bones, tissues, and polymers [33–35, 65–67]. Although such observations have been noted in the past, no work, based on the author's knowledge, has provided the cause of such discrepancies. One possible explanation

for this phenomenon is a potential complex microstructural movement which varies for different modes of deformation, i.e., tension, compression, and flexure.

A possible cause of this microstructural movement and the asymmetry amongst the modes of deformation could be due to the macromolecular chain structure of the cocoa butter. The way the load transfers within these fat structures under different deformation directions might create different behaviours. The micro-pores being considered as inclusions with no reinforcement might disrupt the long fat chain structures within cocoa butter and consequently lead to the differences observed under the different loading conditions. A similar explanation has been reported by Zeybek and Kaynak [67] on their study on synthetic polymers. These findings further confirm the argument that micro-pores inside the chocolate suspension hinder the inelastic/viscoelastic effects in the micro-aerated chocolate.

Due to the microstructural movement observed at the beginning of the experiments resulting in inelastic effects, the Young's modulus of chocolate should be computed from the linear part of the unloading regime in the stress–strain curve. It is important to highlight that an ultrasonic or a three-point bending experiment does not seem to suffer from the microstructural movement effect, providing a good indication of the chocolate's Young's modulus. This is true for all chocolate samples regardless of the level of porosity. The reduced microstructural effect observed during flexure experiments (especially in 0% and 15% chocolate) might be caused due to the fact that a smaller portion of the material is deformed in this test compared to the other two modes of deformation.

Figures 10, 11, and 12, depict that the Young's modulus exhibits a minor dependency on the rate. This dependency is almost eliminated for the 15% micro-aerated chocolate, except for the modulus predicted by the three-point bending experiments. This phenomenon suggests that the material exhibits a viscoplastic material behaviour where the rate dependency is mainly observed in the macroscopic plastic region (see Fig. 6a–c). An exception to this observation regards the data obtained from the three-point bending tests where rate dependency is observed throughout the load–deflection response.

The ultrasound velocity and the wavelength of sound in the case of the non-aerated, 10%, and 15%

micro-aerated chocolate calculated using Eqs. (20) and (21) are summarised in Table 1. Based on the same table, a decreasing trend of c with increasing porosity is depicted, which is common for porous materials [68], and generally, ultrasound methods are known to be sensitive to the presence of voids. The values of the wavelength of sound for all types of chocolate are found to be in the scale of a couple of millimetres which is approximately two orders of magnitude larger than the size of microscopic features found in the micro-aerated chocolate such as the sugar and cocoa particles but also the micro-pores ($\sim$ 40 μm). This suggests that the Young's modulus measured by the ultrasound experiment is the effective Young's modulus of micro-aerated chocolate and is of comparable value to the destructive mechanical experiments. However, in cases where the material contains larger pores at a scale similar to the measured wavelength, this agreement between the flexural modulus and the Young's modulus obtained by the ultrasound measurements might be violated.

The data of flexural modulus, which are computed from the monotonic three-point bending experiments (using Eq. 6), and the data obtained from Eq. (10), are summarised in Fig. 13 for all types of chocolate and two testing speeds. The tensile modulus, which is used to calculate the flexural modulus in Eq. (10), is computed from the initial linear portion of the unloading part of the stress–strain curve from the loading–unloading tensile experiments. Similarly, the compressive modulus, which is used to calculate the constant λ, is obtained from the loading–unloading experiments in compression. The flexural modulus obtained from Eq. (10) (see Fig. 13 the red coloured values) is in good agreement with the values measured from the three-point bending experiments for the 15% micro-aerated chocolate, i.e. < 3% difference.

In the case of the 0% and 10% micro-aerated chocolate, the flexural modulus using Eq. (10) was found to be somewhat lower than the one measured

Table 1 Ultrasound velocity and wavelength of the non-aerated, 10% and 15% micro-aerated chocolate at a constant frequency of 1

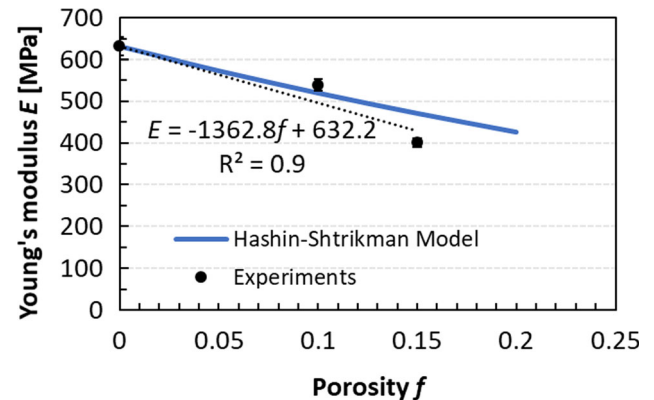| Chocolate	0%	10%	15%
Velocity c [ms^{-1}]	2580	1700	1200
Wavelength λ_u [mm]	2.58	1.70	1.20
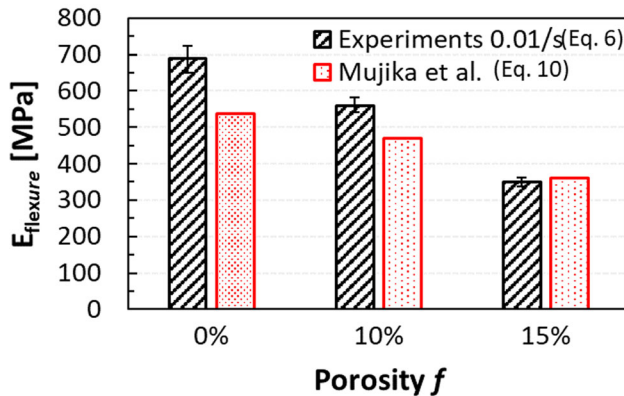
Figure 13 Bar chart showing the flexural modulus obtained from the three-point bending experiments at a testing speed of $\dot{\delta} = 0.85$ mm s^{-1} (equivalent to 0.01 s^{-1}) (see Eq. 6) and the methodology presented by Mujika et al. [48] (see Eq. 10).

Figure 14 Average Young's modulus data obtained from the different mechanical experiments, loading–unloading in compression and tension, three-point bending, and ultrasonic experiments, at a constant strain rate of 0.01 as a function of porosity together with analytical predictions using the Hashin–Shtrikman model used in chocolates by Samaras and Bikos et al. [16, 19].

from the experiments, by 22% and 16% for the 0% and 10% micro-aerated chocolate, respectively. This difference might be caused by the fact that no significant microstructural movement is observed during the three-point bending experiments as opposed to the uniaxial compression and tension tests. Therefore, when the flexural modulus of chocolate is computed using Eq. (10), considering the tensile and compressive moduli from the respective experiments, significant errors are observed. Whereas, in the case of the 15% micro-aerated chocolate, the inelastic microstructural movements are diminishing, and hence, the results of the two methods match perfectly. The agreement between the two methods in the case of the 15% micro-aerated chocolate gives further confidence in all the performed mechanical tests.

Mujika et al. [48] reported that the difference between the tensile modulus computed from Eq. (6) and the direct tensile experiment lie within 5% for unidirectional composites. However, this difference seems to increase drastically when the methodology is applied to multiphase materials, such as chocolates, which exhibit complex microstructural movements under tensile and compressive modes of deformation.

The average values of Young's modulus obtained from the loading–unloading experiments in compression and tension, the three-point bending tests, and the ultrasonic experiments, are summarised in Fig. 14 for all tested materials. As expected, decreasing trends of Young's modulus with increasing porosity are depicted, which is aligned with

reports in the literature for other porous materials [60, 69–71]. More specifically, a maximum decrease of 41% is proposed when the modulus of the non-aerated chocolate is compared to the one of the 15% micro-aerated chocolate. The trend line of the figure proposes an approximate linear relationship between the Young's modulus of chocolate and the porosity. A reasonable agreement is depicted when comparing the experimental data of Fig. 14 to analytical predictions from the Hashin–Shtrikman analytical model (see Eq. 19), which is previously employed for chocolates by Samaras and Bikos et al. [16, 19]. A maximum difference of 12% is reported in the case of the 15% chocolate. The source of this difference is believed to partially originate from the averaging process performed from the different mechanical tests, which might exhibit different sources of error. Nevertheless, the difference between the analytical model and a material which exhibits complex multiphase structure is reasonable and provides further confidence on the measured moduli data for all types of chocolate.

Selecting the correct value of Young's modulus is based on the process of interest and the loading events occurring during that process. More specifically, for instance, during food oral processing, multiaxial loading is reported to occur where compressive and tensile events are found to play a determinant role in the material's fracture. The former type of load is associated by the compressive

action of the teeth, and the latter is linked to the chocolate's fracture due to the lateral deformation of material during mastication. In such a case, details about the stress–strain data in compression and tension are required. All these parameters are needed as input parameters for computational models that simulate the first bite condition [19]. On the other hand, bending events during mastication might be insignificant due to the typical geometry of the food that is masticated and the geometry of the teeth.

On the other hand, in scenarios where the computation of Young's modulus is only important, the three-point bending experiments constitute a quick and reliable way to measure the true value of chocolate's Young's modulus. Such scenarios could be the comparison and correlation of Young's modulus of food with textural properties such as hardness and crumbliness. Several studies have established such links aiming to design food products with controlled sensorial attributes [22, 23, 29, 30]. Flexure experiments are also relevant to snap tests, performed to assess the final quality of chocolate. Easy and reliable experiments to measure the Young's modulus of chocolate are also the ultrasonic tests. This is opposed to the more challenging mechanical experiments such as cyclic compression and tensile experiments, where issues with interfacial friction (in compression) and material gripping (in tension) are usually present.

This is the first time in foods that a conclusive engineering analysis is performed employing different types of mechanical experiments such as compression, tension, flexure, and ultrasound methods, to evaluate the true Young's modulus of complex multiphase materials such as chocolate samples with varying levels of micro-aeration.

Conclusions

A comprehensive engineering analysis on solid chocolate with different levels of micro-aeration was performed employing mechanical destructive and non-destructive experiments to compute the true mechanical properties. The latter are important input parameters to simulate the first bite conditions through computational models and are often linked to textural attributes such as hardness. The results of this work confirmed the requirement that the true modulus of elasticity should be computed from the

unloading part of the uniaxial strain-strain curve during unloading conditions. The comparison of the modulus data amongst different mechanical experiments showed small discrepancies, an effect which is common for polymers and is believed to be due to the way the load transfers across the large fat molecular structures inside the cocoa butter under different deformation directions. This effect is found to be diminishing with increasing porosity. It is argued that the microstructural movement of particles in the chocolate, which is believed to be dependent on the loading condition, is disrupted by the presence of micro-pores and, therefore, diminishes with increasing porosity. More specifically, the micro-pores are believed to disrupt the movement of the long fat molecular chain of the cocoa butter reducing differences shown amongst the different loading conditions. The fact that the fracture strain in compression is drastically higher than the one in tension postulates that the material will predominantly fracture during service due to tensile loads. The Young's modulus of chocolate should be selected based on loading case that is dominant during the event of interest. In cases where a quick estimate of Young's modulus is required, the three-point bending and ultrasonic experiments provide a relatively easy, fast, and reliable way to measure this for chocolate.

Author contributions

DB contributed to conception of the idea, investigation, methodology, formal analysis, writing the original draft, writing, review, and editing of the revised manuscript. MNC contributed to conception of the

idea, writing the original draft, writing, review, and editing of the revised manuscript, project administration, supervision, and funding acquisition. GS, PC, MM, YH, JV, CH, PH, and BL contributed to validation, review and editing the manuscript.

Data availability

The data that support the findings of this study are available from the corresponding author, D. Bikos, upon reasonable request.

Declarations

Conflict of interest The authors declare that they have no known competing financial interests or personal relationships that could have appeared to influence the work presented in this manuscript.

References

[1] Sun Q et al (2019) Failure mechanisms of cross-ply carbon fiber reinforced polymer laminates under longitudinal compression with experimental and computational analyses. Compos B Eng 167:147–160. https://doi.org/10.1016/j.compositesb.2018.12.041

[2] Pimenta S, Pinho ST (2011) Recycling carbon fibre reinforced polymers for structural applications: technology review and market outlook. Waste Manage 31(2):378–392. https://doi.org/10.1016/j.wasman.2010.09.019

[3] Hsieh CL, Tuan WH (2005) Elastic properties of ceramic–metal particulate composites. Mater Sci Eng, A 393(1–2):133–139. https://doi.org/10.1016/j.msea.2004.10.009

[4] Gonabadi H, Oila A, Yadav A, Bull S (2022) Investigation of anisotropy effects in glass fibre reinforced polymer composites on tensile and shear properties using full field strain measurement and finite element multi-scale techniques. J Compos Mater 56(3):507–524. https://doi.org/10.1177/00219983211054232

[5] Li Y, Pimenta S, Singgih J, Nothdurfter S, Schuffenhauer K (2017) Experimental investigation of randomly-oriented tow-based discontinuous composites and their equivalent laminates. Compos Part A Appl Sci Manuf 102:64–75. https://doi.org/10.1016/j.compositesa.2017.06.031

[6] Gomarasca S, Peeters DMJ, Atli-Veltin B, Dransfeld C (2021) Characterising microstructural organisation in unidirectional composites. Compos Sci Technol. https://doi.org/10.1016/j.compscitech.2021.109030

[7] Naderi S, Zhang M (2020) A novel framework for modelling the 3D mesostructure of steel fibre reinforced concrete. Comput Struct. https://doi.org/10.1016/j.compstruc.2020.106251

[8] Chhorn C, Hong SJ, Lee SW (2018) Relationship between compressive and tensile strengths of roller-compacted concrete. J Traffic Transp Eng (English Edition) 5(3):215–223. https://doi.org/10.1016/j.jtte.2017.09.002

[9] Glicerina V, Balestra F, Dalla Rosa M, Romani S (2016) Microstructural and rheological characteristics of dark, milk and white chocolate: a comparative study. J Food Eng 169:165–171. https://doi.org/10.1016/j.jfoodeng.2015.08.011

[10] Beckett ST, Info L, Records M, Read RSC (2019) The science of chocolate. Royal Society of Chemistry, London

[11] Barišić V et al (2019) The chemistry behind chocolate production. Molecules. https://doi.org/10.3390/molecules24173163

[12] Toker OS, Pirouzian HR, Palabiyik I, Konar N (2021) Chocolate flow behavior: composition and process effects. Crit Rev Food Sci Nutr. https://doi.org/10.1080/10408398.2021.1993782

[13] Bikos D et al (2021) Effect of micro-aeration on the mechanical behaviour of chocolates and implications for oral processing. Food Funct 12:4864–4886. https://doi.org/10.1039/D1FO00045D

[14] Bikos D (2022) Effect of micro-aeration on mechanical and thermal properties of chocolate and correlation to oral processing, PhD, Imperial College London, London

[15] Bikos D et al (2022) Experimental and numerical evaluation of the effect of micro-aeration on the thermal properties of chocolate. Food Funct 13(9):4993–5010

[16] Bikos D et al (2021) Effect of structure on the mechanical and physical properties of chocolate considering time scale phenomena occurring during oral processing. Food Struct 31:100244. https://doi.org/10.1016/j.foostr.2021.100244

[17] Samaras G et al (2020) Measurement of molten chocolate friction under simulated tongue-palate kinematics: effect of cocoa solids content and aeration. Curr Res Food Sci 3:304–313. https://doi.org/10.1016/j.crfs.2020.10.002

[18] Haedelt J, Beckett ST, Niranjan K (2007) Bubble-included chocolate: relating structure with sensory response. J Food Sci 72(3):138–142. https://doi.org/10.1111/j.1750-3841.2007.00313.x

[19] Samaras G (2021) Oral processing of micro-aerated chocolates: a computational mechanics, rheological and tribological study. PhD, Imperial College London, London

[20] Skamniotis CG, Elliott M, Charalambides MN (2019) Computer simulations of food oral processing to engineer teeth cleaning. Nat Commun. https://doi.org/10.1038/s41467-019-11288-5

[21] Reinke SK et al (2016) Synchrotron X-Ray microtomography reveals interior microstructure of multicomponent food materials such as chocolate. J Food Eng 174:37–46. https://doi.org/10.1016/j.jfoodeng.2015.11.012

[22] Chen J (2009) Food oral processing- a review. Food Hydrocoll 23(1):1–25. https://doi.org/10.1016/j.foodhyd.2007.11.013

[23] Witt T, Stokes JR (2015) Physics of food structure breakdown and bolus formation during oral processing of hard and soft solids. Curr Opin Food Sci 3:110–117. https://doi.org/10.1016/j.cofs.2015.06.011

[24] van Aken GA, Vingerhoeds MH, de Hoog EHA (2007) Food colloids under oral conditions. Curr Opin Colloid Interface Sci 12:251–262. https://doi.org/10.1016/j.cocis.2007.07.011

[25] Aguayo-Mendoza MG, Chatonidi G, Piqueras-Fiszman B, Stieger M (2021) Linking oral processing behavior to bolus properties and dynamic sensory perception of processed cheeses with bell pepper pieces. Food Qual Prefer. https://doi.org/10.1016/j.foodqual.2020.104084

[26] le Révérend B, Hartmann C (2014) Numerical modeling of human mastication, a simplistic view to design foods adapted to mastication abilities. Physiol Behav 124:61–64. https://doi.org/10.1016/j.physbeh.2013.10.012

[27] Mohammed IK, Charalambides MN, Williams JG, Rasburn J (2014) Modelling the microstructural evolution and fracture of a brittle confectionery wafer in compression. Innov Food Sci Emerg Technol 24:48–60. https://doi.org/10.1016/j.ifset.2013.11.015

[28] Vincent JFV (2004) Application of fracture mechanics to the texture of food. Eng Fail Anal 11(5):695–704. https://doi.org/10.1016/j.engfailanal.2003.11.003

[29] Pascua Y, Koç H, Foegeding EA (2013) Food structure: Roles of mechanical properties and oral processing in determining sensory texture of soft materials. Curr Opin Colloid Interface Sci 18(4):324–333. https://doi.org/10.1016/j.cocis.2013.03.009

[30] Vincent JFV, Saunders DEJ, Beyts P (2002) The use of critical stress intensity factor to quantify 'hardness' and 'crunchiness' objectively. J Texture Stud 33(2):149–159. https://doi.org/10.1111/j.1745-4603.2002.tb01341.x

[31] Çakır E, Daubert CR, Drake MA, Vinyard CJ, Essick G, Foegeding EA (2012) The effect of microstructure on the sensory perception and textural characteristics of whey protein/κ-carrageenan mixed gels. Food Hydrocoll. https://doi.org/10.1016/j.foodhyd.2011.04.011

[32] Harrison SM, Cleary PW (2014) Towards modelling of fluid flow and food breakage by the teeth in the oral cavity using smoothed particle hydrodynamics (SPH). Eur Food Res Technol 238(2):185–215. https://doi.org/10.1007/s00217-013-2077-8

[33] Manta A, Gresil M, Soutis C (2020) Tensile and flexural behaviour of a graphene/epoxy composite: experiments and simulation. J Phys Mater. https://doi.org/10.1088/2515-7639/ab52d8

[34] Demircan O, Al-darkazali A, İnanç, Eskizeybek V (2020) Investigation of the effect of CNTs on the mechanical properties of LPET/glass fiber thermoplastic composites. J Thermoplast Compos Mater 33(12):1652–1673

[35] Shahin A, Barsoum I, Islam MD (2020) Constitutive model calibration of the time and temperature-dependent behavior of high density polyethylene. Polym Test. https://doi.org/10.1016/j.polymertesting.2020.106800

[36] Charalambides MN, Goh SM, Wanigasooriya L, Williams JG, Xiao W (2005) Effect of friction on uniaxial compression of bread dough. J Mater Sci 40(13):3375–3381. https://doi.org/10.1007/s10853-005-2846-2

[37] Charalambides MN, Williams JG, Chakrabarti S (1995) A study of the influence of ageing on the mechanical properties of Cheddar cheese. J Mater Sci 30:3959–3967. https://doi.org/10.1007/BF00360694

[38] Lasalle A, Guizard C, Deville S, Rossignol F, Carles P (2011) Investigating the dispersion state of alumina suspensions: contribution of cryo-field-emission gun scanning electron microscopy characterizations. J Am Ceram Soc 94(1):244–249. https://doi.org/10.1111/j.1551-2916.2010.04034.x

[39] Mohammed MAP (2012) Mechanical characterisation, processing and microstructure of wheat flour dough. London

[40] Sánchez-Ayala A, Farias-Neto A, Campanha NH, Rodrigues Garcia RCM (2013) Relationship between chewing rate and masticatory performance. Cranio J Craniomandib Pract 31(2):118–122

[41] Meullenet JF, Finney ML, Gaud M (2002) Measurement of biting velocities, and predetermined and individual cross-head speed instrumental imitative tests for predicting cheese hardness. J Texture Stud 33(1):45–58. https://doi.org/10.1111/j.1745-4603.2002.tb01334.x

[42] Carvalho-da-silva AM, van Damme I, Wolf B, Hort J (2011) Characterisation of chocolate eating behaviour. Physiol Behav 104(5):929–933. https://doi.org/10.1016/j.physbeh.2011.06.001

[43] Barnes HA (1999) The yield stress—a review or 'παντα ρει'—everything flows? J Nonnewton Fluid Mech 81(1–2):133–178. https://doi.org/10.1016/S0377-0257(98)00094-9

[44] Flinn RA, Trojan PK, Trojan F (1975) Engineering materials and their applications. Houghton Mifflin, Boston

[45] Ross CTF (1999) Mechanics of solids, 1st edn. Woodhead Publishing, Sawston

[46] ASTM International, "D7264/D7264M − 15 - standard test method for flexural properties of polymer matrix composite materials," ASTM Standards, vol. i, pp. 1–11, 2007, https://doi.org/10.1520/D7264

[47] Mujika F (2007) On the effect of shear and local deformation in three-point bending tests. Polym Test 26(7):869–877. https://doi.org/10.1016/j.polymertesting.2007.06.002

[48] Mujika F, Carbajal N, Arrese A, Mondragon I (2006) Determination of tensile and compressive moduli by flexural tests. Polym Test 25(6):766–771. https://doi.org/10.1016/j.polymertesting.2006.05.003

[49] Goh SM, Charalambides MN, Williams JG (2003) Large strain time dependent behavior of cheese. J Rheol (N Y N Y) 47(3):701–716. https://doi.org/10.1122/1.1562153

[50] Luczynski KW, Steiger-Thirsfeld A, Bernardi J, Eberhard-steiner J, Hellmich C (2015) Extracellular bone matrix exhibits hardening elastoplasticity and more than double cortical strength: Evidence from homogeneous compression of non-tapered single micron-sized pillars welded to a rigid substrate. J Mech Behav Biomed Mater 52:51–62. https://doi.org/10.1016/j.jmbbm.2015.03.001

[51] Zhao S et al (2018) Standardizing compression testing for measuring the stiffness of human bone. Bone Joint Res 7(8):524–538. https://doi.org/10.1302/2046-3758.78.BJR-2018-0025.R1

[52] Povey MJW (1998) Ultrasonics of food. Contemp Phys 39(6):467–478. https://doi.org/10.1080/001075198181784

[53] Mcclements DJ, Povey MJW (1992) Ultrasonic analysis of edible fats and oils. Ultrasonics 30(6):383

[54] Afoakwa EO, Paterson A, Fowler M, Vieira J (2009) Microstructure and mechanical properties related to particle size distribution and composition in dark chocolate. Int J Food Sci Technol 44(1):111–119. https://doi.org/10.1111/j.1365-2621.2007.01677.x

[55] Hibbeler RC (2018) Mechanics of materials, 10th ed. Pearson, 2018. [Online]. Available: www.pearsonglobaleditions.com/hibbeler

[56] Matsagar V (2015) Advances in structural engineering: mechanics. Springer, Berlin

[57] Bhagyashekar MS, Rao RMVGK (2010) Characterization of mechanical behavior of metallic and non-metallic particulate filled epoxy matrix composites. J Reinf Plast Compos 29(1):30–42. https://doi.org/10.1177/0731684408095034

[58] Ezema Ike-Eze IC, Uyor UO, Aigbodion VS, Omah AD, Ude SN, Daniel-Nkpume CC (2019) Tensile and compressive strength of palm kernel shell particle reinforced polyester composites. Mater Res Express 6(11):115335. https://doi.org/10.1088/2053-1591/ab4afa

[59] Ahmad SN, Hashim J, Ghazali MI (2005) The Effects of Porosity on Mechanical Properties of Cast Discontinuous Reinforced Metal-Matrix Composite. J Compos Mater 39(5):451–466. https://doi.org/10.1177/0021998305047096

[60] el Ghezal MI, Maalej Y, Doghri I (2013) Micromechanical models for porous and cellular materials in linear elasticity and viscoelasticity. Comput Mater Sci 70:51–70. https://doi.org/10.1016/j.commatsci.2012.12.021

[61] Bernardo V, Loock F, Martin-de Leon J, Fleck NA, Rodriguez-Perez MA (2019) Mechanical properties of PMMA-sepiolite nanocellular materials with a bimodal cellular structure. Macromol Mater Eng. https://doi.org/10.1002/mame.201900041

[62] Chen X, Wu S, Zhou J (2013) Influence of porosity on compressive and tensile strength of cement mortar. Constr Build Mater 40:869–874. https://doi.org/10.1016/j.conbuildmat.2012.11.072

[63] Gonzalez-Gutierrez J, Scanlon MG (2012) Rheology and Mechanical Properties of Fats. Struct Funct Anal Edible Fats. https://doi.org/10.1016/B978-0-12-814041-3.00005-8

[64] Hellmich C, Katti D (2015) Multiscale mechanics of biological, bioinspired, and biomedical materials. MRS Bull 40(4):309–313. https://doi.org/10.1557/mrs.2015.65

[65] Sachin SR, Kannan TK, Rajasekar R (2020) Effect of wood particulate size on the mechanical properties of PLA biocomposite. Pigm Resin Technol 49(6):465–472. https://doi.org/10.1108/PRT-12-2019-0117

[66] Li BW, Zhao HP, Feng XQ, Guo WW, Shan SC (2010) Experimental study on the mechanical properties of the horn sheaths from cattle. J Exp Biol 213(3):479–486. https://doi.org/10.1242/jeb.035428

[67] Meyva-Zeybek Y, Kaynak C (2021) A comparative study for the behavior of 3D-printed and compression molded PLA/ POSS nanocomposites. J Appl Polym Sci 138(16):1–11. https://doi.org/10.1002/app.50246

[68] Ma W, Liu F (2012) Effects of porosity on ultrasonic characteristic parameters and mechanical properties of glass fiber reinforced composites. Int J Mod Phys Conf Ser 06:646–651. https://doi.org/10.1142/s2010194512003911

[69] Kováčik J (1999) Correlation between Young's modulus and porosity in porous materials. J Mater Sci Lett 18:1007–1010. https://doi.org/10.1023/A:1006669914946

[70] Wang JC (1984) Young's modulus of porous materials - Part 1 Theoretical derivation of modulus-porosity correlation. J Mater Sci 19(3):801–808. https://doi.org/10.1007/BF00540451

[71] Nakajima H (2007) Fabrication, properties and application of porous metals with directional pores. Prog Mater Sci 52(7):1091–1173. https://doi.org/10.1016/j.pmatsci.2006.09.001

Publisher's Note Springer Nature remains neutral with regard to jurisdictional claims in published maps and institutional affiliations.